

Article

Correlation Study between the Mechanical Property of the Square Cone Energy-Absorbing Structure and Collision Energy Distribution for Urban Rail Trains

Ping Xu ^{1,2,3,*}, Ao Wang ^{1,2,3}, Liting Yang ^{1,2,3}, Quanwei Che ⁴ and Chengxing Yang ^{1,2,3}

- ¹ Key Laboratory of Traffic Safety on Track, Ministry of Education, School of Traffic & Transportation Engineering, Central South University, Changsha 410075, China
- ² Joint International Research Laboratory of Key Technology for Rail Traffic Safety, School of Traffic & Transportation Engineering, Central South University, Changsha 410075, China
- ³ National & Local Joint Engineering Research Center of Safety Technology for Rail Vehicle, Central South University, Changsha 410075, China
- ⁴ CRRC Qingdao Sifang Co., Ltd., Qingdao 266111, China
- * Correspondence: xuping@csu.edu.cn

Abstract: In order to study the influence of the square cone energy-absorbing structure of urban rail trains on the collision energy distribution of trains during the collision process, an eight-marshalling train crash dynamics model was established, and the force–displacement energy-absorbing characteristic curve of the anti-climbing structure was obtained through a full-scale impact experiment. According to the characteristics of the curve, the influence of the initial peak force, the platform force and the slope of the platform force of the anti-climbing energy-absorbing device on the energy absorption of the train collision under a 25 km/h condition was studied. Based on this, the multi-objective genetic algorithm was used to optimize the overall energy distribution scheme of the train. The results showed that the changes in the initial peak force, the platform force and the slope of the platform force will lead to changes in the energy absorption of the four-section moving train and the four-section stationary train that are closer to the collision interface, and the other is almost unchanged. Through the optimized design, the energy absorption of the head car impact interface is increased by 0.74%, the energy absorption of the first impact interface of the middle cars is reduced by 3.36% and the third impact interface of the middle cars is increased by 9.17%. The distribution of the collision energy of the train is more reasonable. At the same time, the deformation of the middle car body is reduced, and the utilization efficiency of the overall energy-absorbing structure of the train is improved.

Keywords: urban rail trains; square cone energy-absorbing structure; collision energy distribution; multi-objective optimization



Citation: Xu, P.; Wang, A.; Yang, L.; Che, Q.; Yang, C. Correlation Study between the Mechanical Property of the Square Cone Energy-Absorbing Structure and Collision Energy Distribution for Urban Rail Trains. *Machines* **2022**, *10*, 747. <https://doi.org/10.3390/machines10090747>

Received: 22 July 2022

Accepted: 23 August 2022

Published: 29 August 2022

Publisher's Note: MDPI stays neutral with regard to jurisdictional claims in published maps and institutional affiliations.



Copyright: © 2022 by the authors. Licensee MDPI, Basel, Switzerland. This article is an open access article distributed under the terms and conditions of the Creative Commons Attribution (CC BY) license (<https://creativecommons.org/licenses/by/4.0/>).

1. Introduction

With the improvement of the speed of urban rail trains, more and more attention has been paid to the safety of train operation. The energy-absorbing structure is the key structure of the passive safety of the train, which has a great impact on the collision process. As one of the most common energy-absorbing structures, thin-walled tubes can achieve energy absorption through the expansion, shrinkage, splitting and cutting of the tube body, and improve the energy-absorbing efficiency and space utilization through different combinations of various energy-absorbing structures [1]. Many scholars have studied its compression mode and energy absorption characteristics based on the crashworthiness [2–7] and carrying out parameter design and optimization for different forms of energy absorption structures [8–10]. Based on compression experiments on Nomex honeycombs, Xie et al. [11] verified the equivalent numerical model for them, which was applied to anti-climbing

energy-absorbing devices, and established the finite element model (FEM) for it in Hypermesh, and then analyzed the effects of parameters of different honeycombs through LS-DYNA. Xu et al. [12] came up with a new cut-out groove design, verified the finite element model through dynamic impact experiments, established response surface models of energy absorption and initial peak crushing force with groove dimensions, and used an adaptive simulated annealing algorithm to carry out optimized design, so that the initial peak crushing force was greatly reduced. Wang et al. [13] designed a cutting energy-absorbing structure, validated the finite element model, which used Johnson–Cook material by using cutting collision experiment data, discussed the effects of the cutting depth, cutting width and cutting knife rake angle on the energy absorbed (EA) and the peak cutting force (PCF), and used multi-objective particle swarm optimization algorithm to obtain the maximum EA and minimum PCF. Chen et al. [14] proposed a longitudinal windowed design to improve the crashworthiness of the multi-cell energy-absorbing structure at the front end of a high-speed train, and established the finite element model by LS-DYNA. On this basis, the radial basis function (RBF) and deep belief network (DBN) were combined to form a hybrid surrogate model, using the multi-objective genetic algorithm to obtain the best design of the thickness of the structure, and the size and location of the windows. Guo et al. [15] proposed a variable stiffness collision post (VSCP) structure based on a uniform stiffness collision post (USCP) structure, built the finite element model and verified it through the impact experiment. Furthermore, they studied the effects of the stiffness parameters of VSCP on the specific energy absorption response and the area of intrusion response by fitting data through response surface models and realizing multi-objective optimization through a global response search method. These studies above are mainly based on the finite element method. Except for these, there are also scholars using the dynamic method to study the energy-absorbing configuration characteristics of the energy-absorbing structure [16–19]. Zhao et al. [20] introduced a novel design method of the impact zone based on the concept of linear impact force. She selected the linear impact force slope of energy-absorbing devices as design variables, and the total mean acceleration along the train (TMA) and the total crash displacement (TS) were set as objectives. A three-dimensional dynamic model of train collision was constructed and validated, and used the multi-objective particle swarm optimization to seek an optimal design. Ambrósio et al. [21] obtained the force–displacement curve of energy-absorbing structures, which included the couplers, buffers and other structural devices from the experiment and simulation results, and then using these curves to correct the multibody dynamics model. Xu et al. [22] established a full-size three-dimensional model of a subway vehicle using the multibody dynamics software MADYMO, scaled down the simulation based on the model and verified it by comparing it with the scaled model test results. Then, they studied the effects of the marshalling, mass and crushing tube’s plastic deformation platform force on the energy absorption of subway vehicles.

Most of the prior studies paid much attention to the energy-absorbing structure itself, such as analyzing the relationship between geometry structural parameters and mechanical properties, and some further studied its effect on the dynamic response of the individual vehicle, such as acceleration, velocity, crash displacement and energy absorption. Few researches combined the energy-absorbing structure with the overall train collision energy distribution and studied their correlation. Some scholars also investigated the effect of impact force on dynamic responses of multi-marshalling trains, but many of them started from the simulation result directly. Therefore, in order to study the influence of the energy-absorbing structure of urban rail trains on the overall collision energy distribution, this paper takes the square cone anti-climbing energy-absorbing structure of urban rail trains as the research object, and adopts the multibody dynamics method to establish the longitudinal collision of an eight-marshalling train model. Through the dynamic impact experiment, we obtain the force–displacement curve of the square cone energy-absorbing structure, and then extract three mechanical characteristic parameters from it. The dynamic model is used to analyze the influence of the mechanical characteristic parameters of

the square cone anti-climbing energy-absorbing structure on the overall collision energy distribution of the train under train collision scenario 1 at 25 km/h, as stipulated in collision standard EN15227:2020 [23].

2. Train Collision Energy Distribution and Square Cone Energy-Absorbing Structure

2.1. Train Collision Energy Distribution

The core goal of vehicle crashworthiness design is to maximize the safety of the occupants and the integrity of other structures of the train, and let the energy-absorbing structure produce a controllable and orderly deformation during the collision process to absorb the collision energy through adding the energy-absorbing structure into the train body and rationally designing the longitudinal stiffness of different parts. As shown in Figure 1, when the subway train collides, the coupler buffer device is the energy-absorbing element that comes into contact first. In the beginning, the draft gear will act, and then the collapse tube begins to absorb energy. After the collapse tube acts completely, the coupler shears and then fails. For the head car, after the coupler shears, the anti-climbing energy-absorbing device acts and absorbs energy. Finally, plastic deformation occurs at the front end of the car body to absorb energy; while for the middle car, because it does not have the anti-climbing energy absorption device, if the energy is not dissipated after the collapse tube is fully applied, the car body will directly deform and participate in energy absorption, which may affect the living space of passengers and the integrity of the vehicle. However, in reality the condition is much more complicated. When a train collision occurs, it does not mean that the energy-absorbing structure of the head car will be fully utilized, and then the energy-absorbing structure of the next middle car starts to act. In fact, after the draft gear of the head car has acted completely, the energy-absorbing structure of the middle car and the collapse tube of the head car just begin to absorb energy together. Moreover, even before the collapse tube has been made full use of, structures for the energy absorption of the following middle cars will participate in the process of energy absorption and dissipation. In many train collision accidents, several sections of vehicles close to the collision interface are deformed to a large extent, but the energy-absorbing structure of the subsequent vehicles basically does not function to absorb energy, which means the train collision energy absorption and dissipation is not reasonable. It can also be seen that, in the crashworthiness design, the dissipation and distribution of energy is a very important part. Regarding train collision energy distribution, both Europe and the United States have this emphasized and highlighted in their standards. The European collision standard EN15227:2020 emphasizes the multi-level energy absorption criterion, which clearly stipulates “absorb collision energy in a controlled manner”; The American Railroad Administration (FRA) proposed the idea of crash energy management (CEM) and applied it to crash standard CFR49. Based on this, a large number of simulation studies were carried out and many crash experiment reports were released [24,25]. In recent years, some Chinese scholars have also conducted relevant research on train collision energy management and configuration based on the collision scenario [26,27], but they pay more attention to mean acceleration, instantaneous acceleration and longitudinal deformation, etc., and there are few studies on the overall collision energy distribution. In this paper, starting from the square cone anti-climbing energy-absorbing structure, the influence of its mechanical parameters on the overall collision energy distribution of the train is analyzed, and then the distribution of the collision energy of the train in each interface is optimized, so as to realize reasonable energy absorption and make the most of the energy-absorbing structure.

2.2. Square Cone Energy-Absorbing Structure for Urban Rail Trains

In the collision of urban rail trains, its energy absorption is mainly completed by the coupler buffer device, anti-climbing device and the deformable area of the car body. For the coupler buffer device, its compression stroke is short and the force is not high, so its energy absorption capacity is limited. While for the car body, we hope that there will be as little deformation as possible during the collision process. Therefore, the anti-climbing

device is the main energy-absorbing structure of the urban rail train, and its importance to the safety of the train is self-evident.

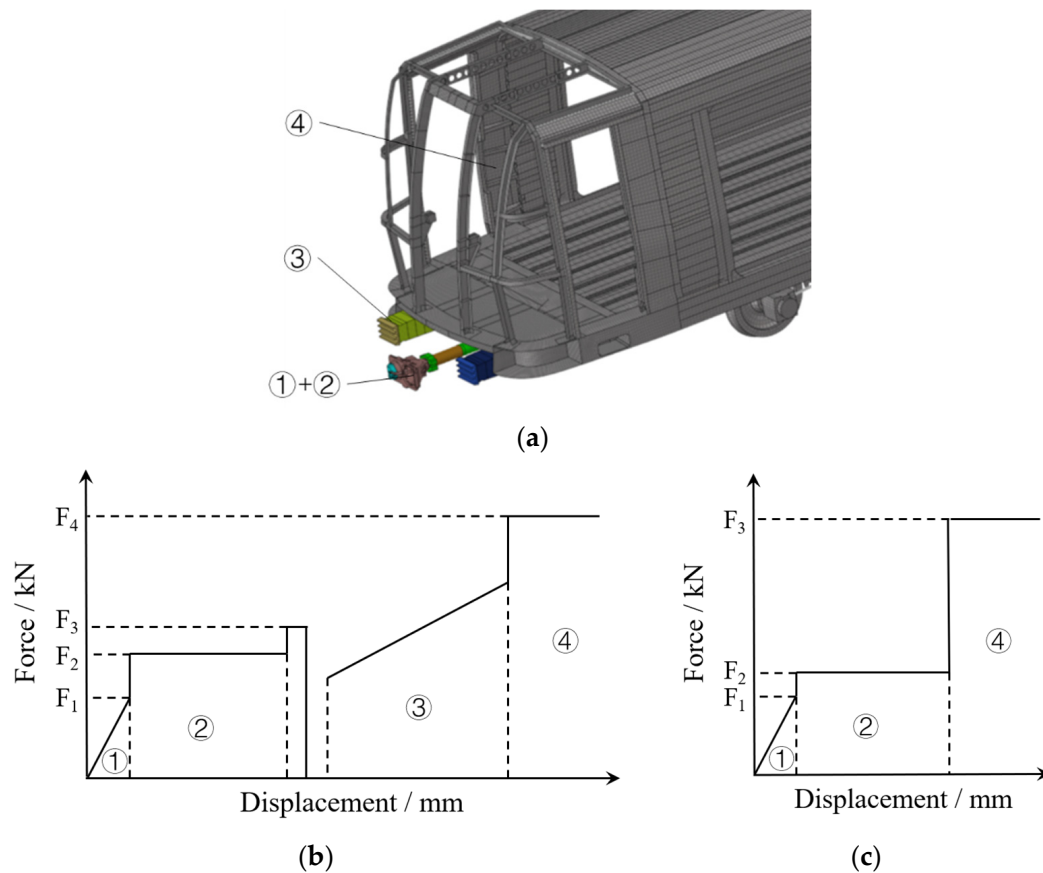


Figure 1. Energy absorption sequence of energy-absorbing structures: (a) energy-absorbing structures: ① draft gear ② collapse tube ③ anti-climbing device ④ car body, (b) the head car, (c) the middle car.

In urban rail trains, it is usually installed on both sides of the front end of the car body, and arranged symmetrically along the longitudinal centerline. The square cone energy-absorbing structure in this paper is composed of anti-climbing teeth, conical thin-walled tubes, front-end plate, rear-end plate, thin-walled diaphragms, aluminum honeycomb structures and guide tubes, as shown in Figure 2.

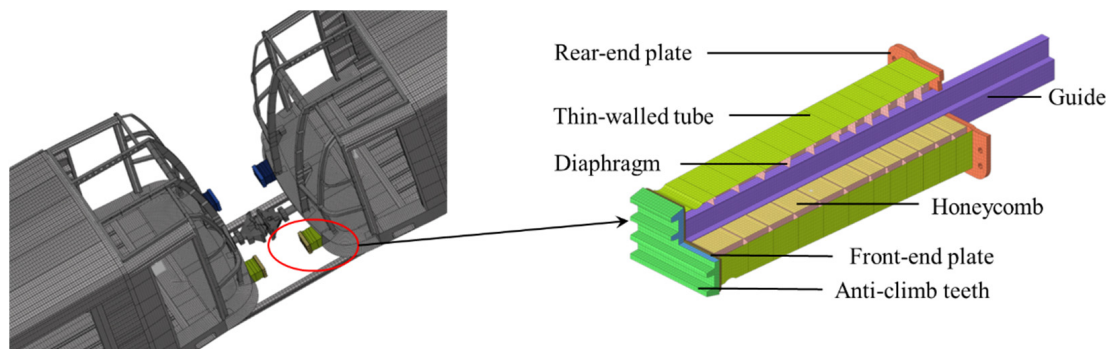


Figure 2. Schematic diagram of the square cone anti-climbing energy-absorbing structure.

3. Collision Dynamics Model of Urban Rail Trains

3.1. Dynamic Model of Train Longitudinal Collision

In this paper, according to the collision scenario 1 of EN15227, the stationary train is impacted by the moving train with a speed of 25 km/h. The collision between two identical railway multiple units has been simulated using Motionview software, as shown in Figure 3, where M represents the moving car, S represents the stationary car and M0 and S0 represent the head car of the moving train and stationary train, respectively. M1 and S1 represent the first middle car of the moving train and the stationary train, respectively, and so on. The collision mass of the vehicle is the sum of the full weight of the vehicle during normal operation and the mass of 50% of the seats of the passengers. Except for the two head cars, whose mass is 43.125 t, the rest of the cars are 45 t. The collision mass distribution is shown in Table 1. The friction coefficient between vehicles is set to 0.2, and under braking condition, the dynamic friction coefficient and static friction coefficient between the wheels and the rail are both set to 0.013.

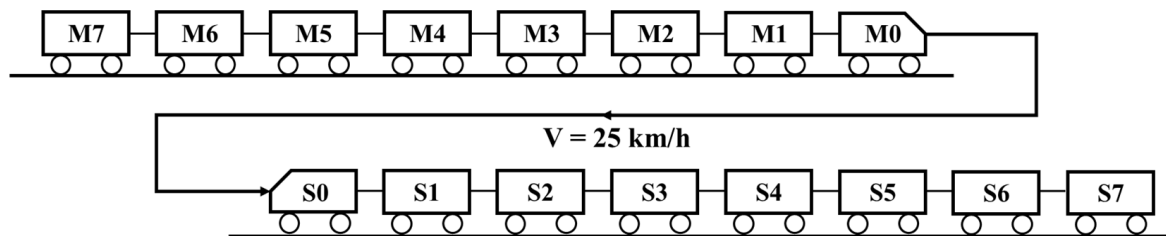


Figure 3. Dynamic collision model of vehicle system.

Table 1. Vehicle mass distribution.

Car No.	0	1	2	3	4	5	6	7
Mass/t	43.125	45	45	45	45	45	45	45

The energy-absorbing structure between trains are simulated by nonlinear hysteresis springs. In addition, the energy-absorbing structure of the head car (i.e., M0 and S0) includes two parts, the coupler buffer device and the anti-climbing energy-absorbing structure, while it only has the coupler buffer device for the middle cars. The energy absorption characteristic curves of the coupler buffer device of the head car and the middle car are shown in Figure 4a,b, respectively.

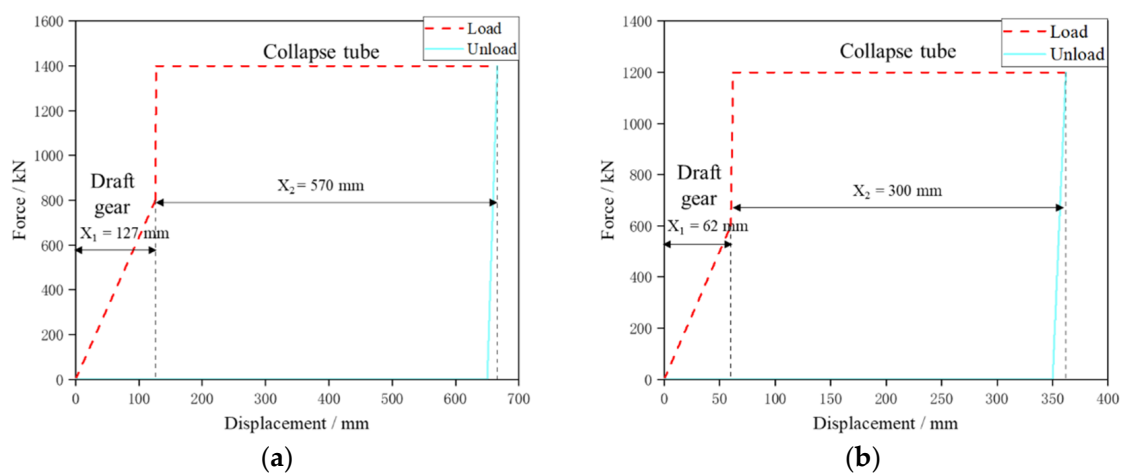


Figure 4. Coupler buffer device energy absorption characteristic curve: (a) the head car, (b) the middle car.

3.2. Force–Displacement Curve of Square Cone Anti-Climbing Energy-Absorbing Structure

In order to obtain the force–displacement curve of the square cone anti-climbing energy-absorbing structure and then study the influence of the mechanical characteristic parameters of it on the overall collision energy distribution of the train, we performed a full-scale collision experiment of this energy-absorbing structure on the standard track, as shown in Figure 5.

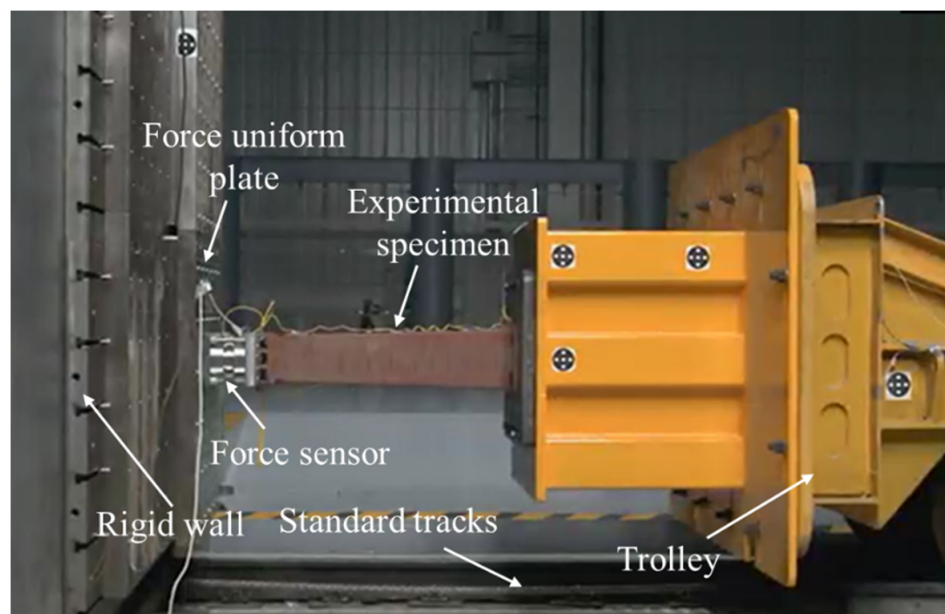


Figure 5. The dynamic impact experiment setup [28].

The whole experimental system consists of rigid walls, uniform force plates, force sensors, an experimental specimen, speedometers, an impact trolley, launch devices and high-speed cameras. The energy-absorbing structure was fixed on the front end of the trolley, and the total weight of the trolley after installation was 16.1 t. The method followed was to drag the trolley to the far end, and then drive the trolley to hit the rigid wall with an initial speed of 17.9 km/h through the motor drive device. The displacement–time curve and the force–time curve of the energy-absorbing structure was obtained with the high-speed camera and the force sensor, respectively. After orthogonal processing of the two, and combined with the previous simulation research of our research group, the force–displacement curve of a single square cone energy-absorbing structure was obtained, as shown in Figure 6a. From Figure 6a, we can see the change trend of the curve. At the beginning of the experiment, the anti-climb teeth of the structure contacted with the rigid wall, the contact force increased to over 500 kN rapidly within about 10 mm of the compress stroke, and then decreased at about the same rate. As the impact progressed further, honeycombs started to be compressed one after another, the force–displacement curve began to show a clear rise in fluctuations, and this segment was relatively stable. After honeycombs were compressed completely, the structure began to unload and no longer absorb energy, and the trolley rebounded. In order to study the relationship between the mechanical property of the square cone energy-absorbing structure and the overall energy distribution of the train collision, three parameters: the initial peak force F_{max} , the platform force F and the slope of platform force K , were extracted from the force–displacement characteristic curve to study their influence on urban rail trains, which are shown in Figure 6b.

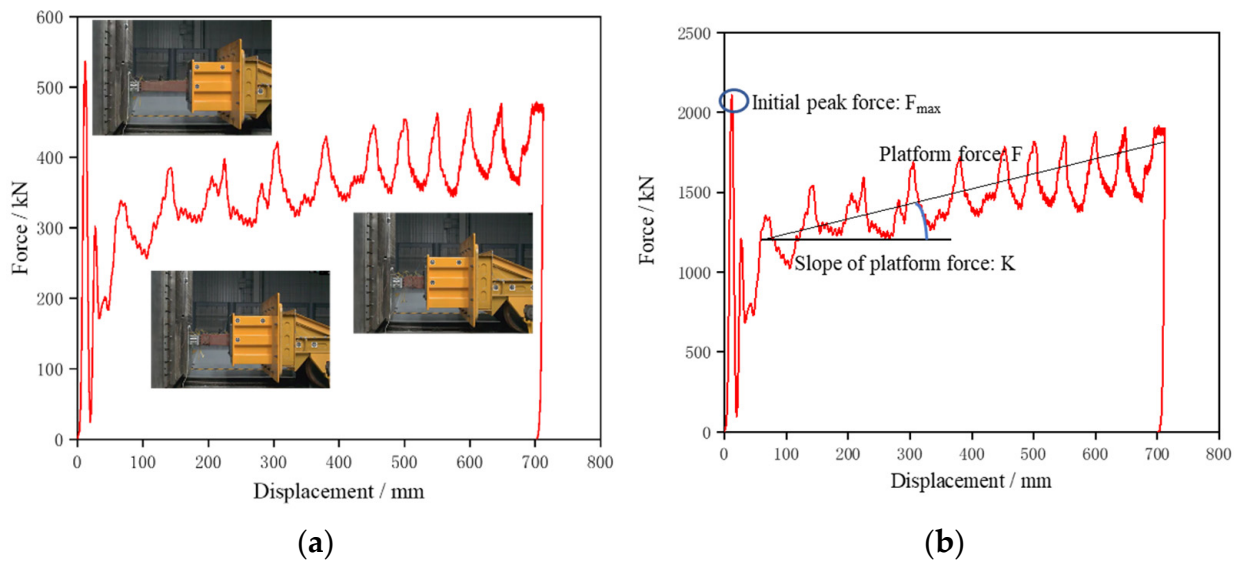


Figure 6. Force–displacement curve of square cone anti-climbing energy-absorbing structure: (a) the single square cone structure curve [29], (b) force–displacement curve in the model.

3.3. Simulation Calculation Result Analysis

According to the collision scenario in 3.1, the Motionview multibody dynamic software was used to conduct the collision simulation calculation, and the result was shown in Figure 7. The speed of the moving trains continued to decrease, and the speed of the stationary trains continued to rise, and the two trains gradually approached. At approximately $t = 0.85$ s, the two trains had the same speed, and then moved forward at the same speed under the action of friction.

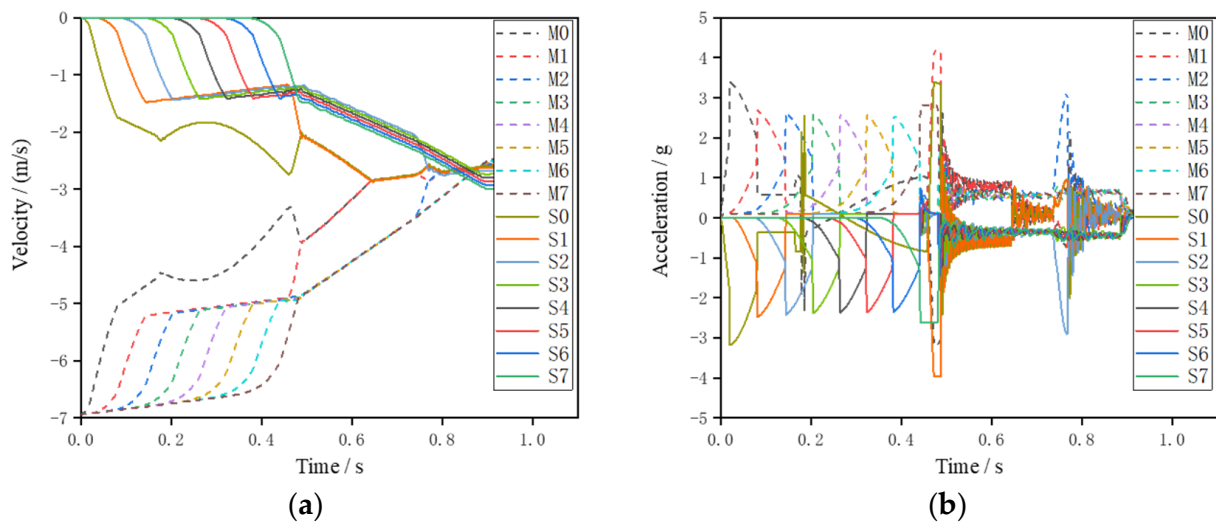


Figure 7. Velocity–time and acceleration–time graphs for each vehicle: (a) velocity–time, (b) acceleration–time.

The compression stroke and energy absorption of each collision interface are shown in Table 2. When the collision occurred, the strokes of the head car impacted interface M0–S0, and the interfaces M1–M0, M2–M1, S0–S1, and S1–S2 were relatively large. The stroke of the anti-climbing device exceeded 700 mm and reached 706.4 mm, and the coupling buffer devices of M1, M2, and S1 had a complete function of the collapse tube, indicating that their energy absorption capacity had been fully utilized. The energy absorption of each collision interface is shown in Figure 8 (the absorption energy of the collision interface M0–S0 has been averaged, denoted by M0 and S0, respectively). From this, we can see that the head

car impact interface absorbed the most energy, the energy absorption of each of the four subsequent collision interfaces exceeded or was around 400 kJ, and for the other remaining collision interfaces, the energy absorbed by each of them was less than or around 100 kJ. The total kinetic energy of the train before the collision was 8.64 MJ. After the collision, the energy absorbed by the energy-absorbing structure was 4.22 MJ in total, accounting for 48.84% of the total energy. In addition, the kinetic energy was mainly absorbed by the energy-absorbing structure of the eight-section cars, which are closer to the interface for collision.

Table 2. Simulation results.

Impact Interface	Total Stroke (mm)	Draft Gear Stroke (mm)	Collapse Tube Stroke (mm)	Energy Absorption (kJ)
M7–M6	81.94	62	19.94	43.64
M6–M5	92.17	62	30.17	55.89
M5–M4	92.58	62	30.58	56.38
M4–M3	93.71	62	31.71	57.64
M3–M2	133.19	62	71.19	104.98
M2–M1	376.88	62	314.88	407.40
M1–M0	390.11	62	328.11	445.96
M0–S0	1403.40	127	570.00	1973.82
S0–S1	380.23	62	318.23	434.63
S1–S2	347.63	62	285.63	375.33
S2–S3	94.98	62	32.98	67.35
S3–S4	82.95	62	20.95	51.41
S4–S5	81.97	62	19.97	50.77
S5–S6	81.26	62	19.26	50.28
S6–S7	72.44	62	10.44	39.93

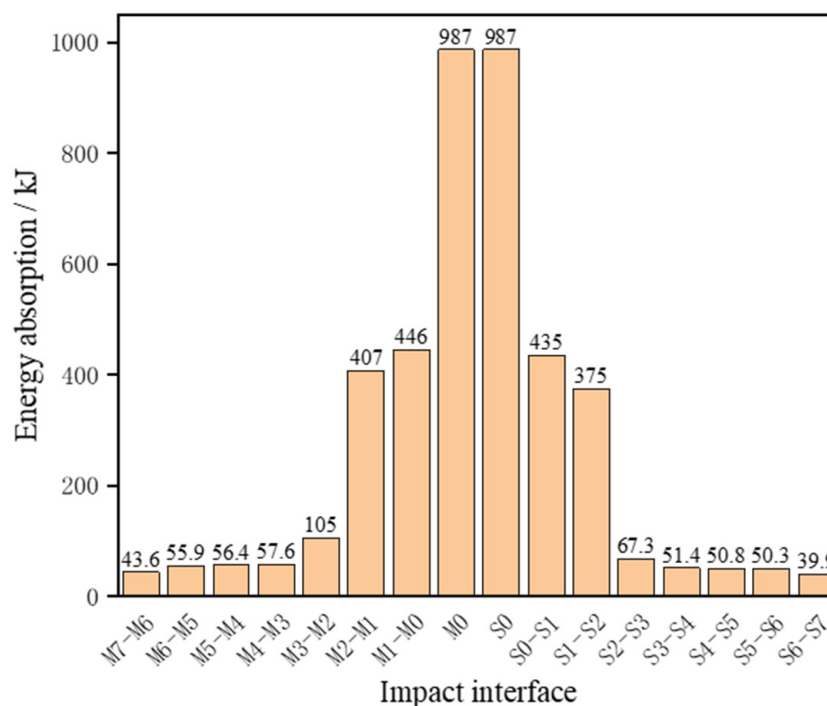


Figure 8. Energy absorbed by each interface.

4. Parameter Analysis

4.1. Influence of the Initial Peak Force

Keeping the platform force F of the square cone anti-climbing energy-absorbing structure at 1650 kN and the platform force slope K unchanged at 1.000, just the same as the simulation condition in 3.3, and changing the initial peak force F_{\max} from 1906 kN to

2306 kN at intervals of 40 kN generated 11 sets of parameters, namely Case1–Case11, to carry out a simulation calculation. The influence of the initial peak force change on the energy absorption of each collision interface is shown in Figure 9 (the absorption energy of the impact interface M0–S0 has been equally divided into the absorption energy of S0 and M0, and the same for the latter figure in this paper).

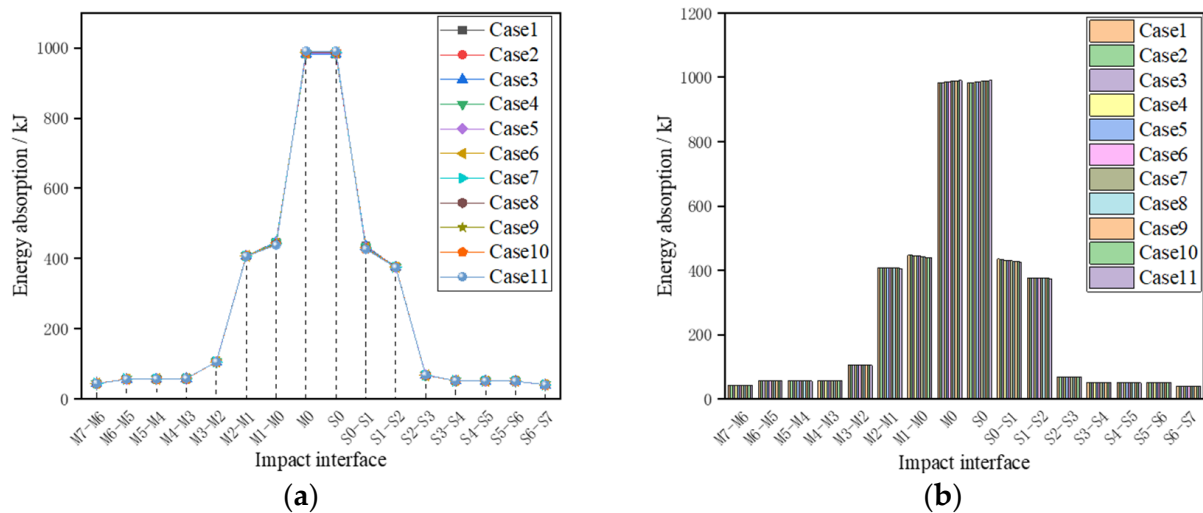


Figure 9. Influence of initial peak force change on overall train collision energy: (a) broken line graph, (b) bar chart.

It can be seen from the line graph that, except for the M0–S0, M1–M0 and S0–S1 impact interfaces, the change in F_{max} of the anti-climbing energy-absorbing structure has basically no effect on other interfaces of the train energy broken line. Further observation of the bar chart shows that the energy absorption of the head car impact interface M0–S0 will increase with the variation in F_{max} , while the energy absorption of the two middle car interfaces M1–M0 and S0–S1 will reduce.

Figure 10 shows the change in the energy absorption of the head cars S0 and M0, and the middle car impact interfaces M1–M0 and S0–S1 with the initial peak force. The energy absorption of the head car increased from 981 kJ to 991 kJ with the increase in the initial peak force, while the energy absorption of the middle car impact interfaces M1–M0 and S0–S1 will reduce with the variation in the initial peak force F_{max} . Combined with Figure 11, it can be seen that the increase in the initial peak force of the square cone anti-climbing energy-absorbing structure will lead to a slight decrease in the energy absorption of the first middle car interfaces M1–M0 and S0–S1, and the reduced energy absorption flows to the leading cars S0 and M0.

4.2. Influence of the Platform Force

Keeping the initial peak force $F_{max} = 2106$ kN and the platform force slope $K = 1.000$ of the square cone anti-climbing energy-absorbing structure unchanged, and changing the platform force F from 1450 kN to 1850 kN at intervals of 40 kN gives 11 sets of parameters Case1–Case11 to perform a simulation calculation separately. The results are shown in Figure 12. It can be seen from the broken line diagram that, with the increase in the platform force F of the energy absorption structure, the broken line of the train energy has varied significantly, which indicates that the variation in the platform force has a great impact on the energy distribution of the train. Furthermore, from the bar chart, we can see that the energy absorption of the head car impact interface M0–S0 and the six middle interfaces, which are close to the collision center, change significantly, while the absorption energy of the other interfaces basically does not change.

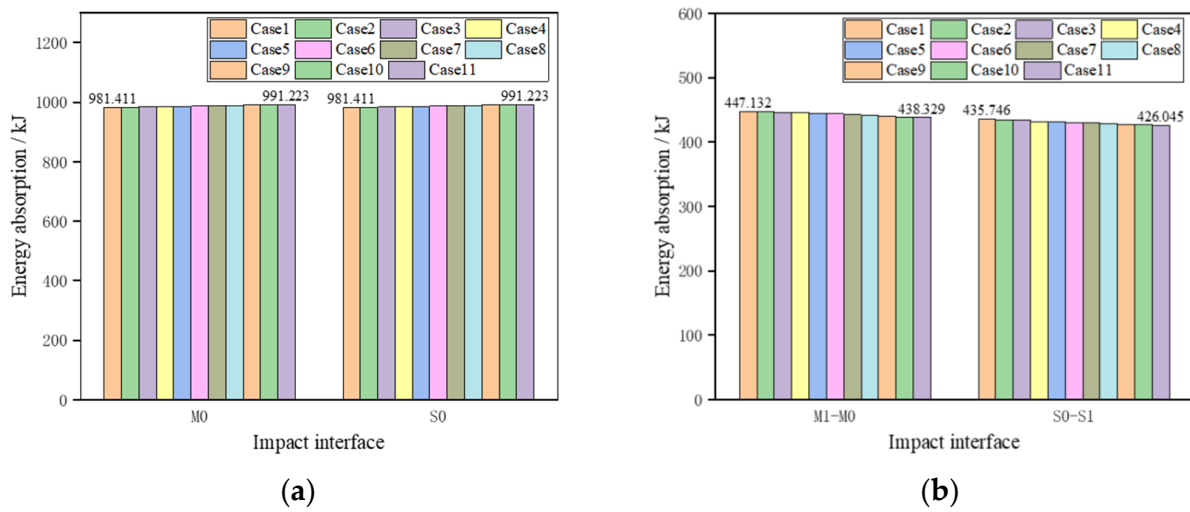


Figure 10. Influence of the initial peak force F_{max} change on specific impact interfaces: (a) head car, (b) the first middle car interfaces: M1–M0 and S0–S1.

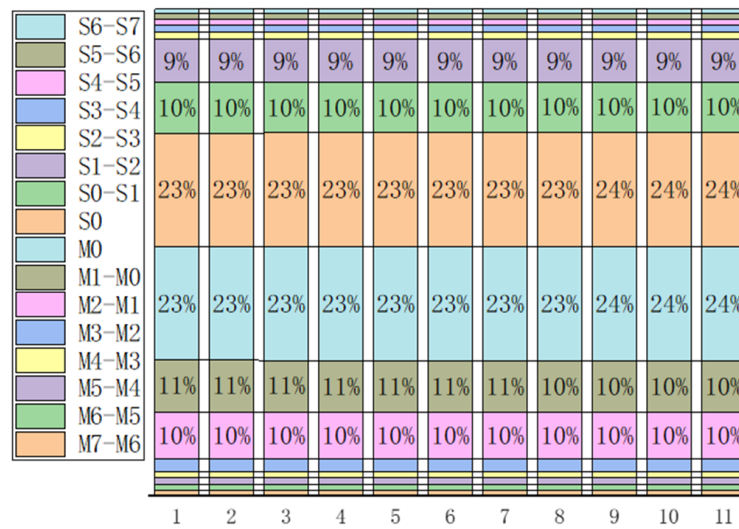


Figure 11. Energy distribution at each interface with the change in the initial peak force.

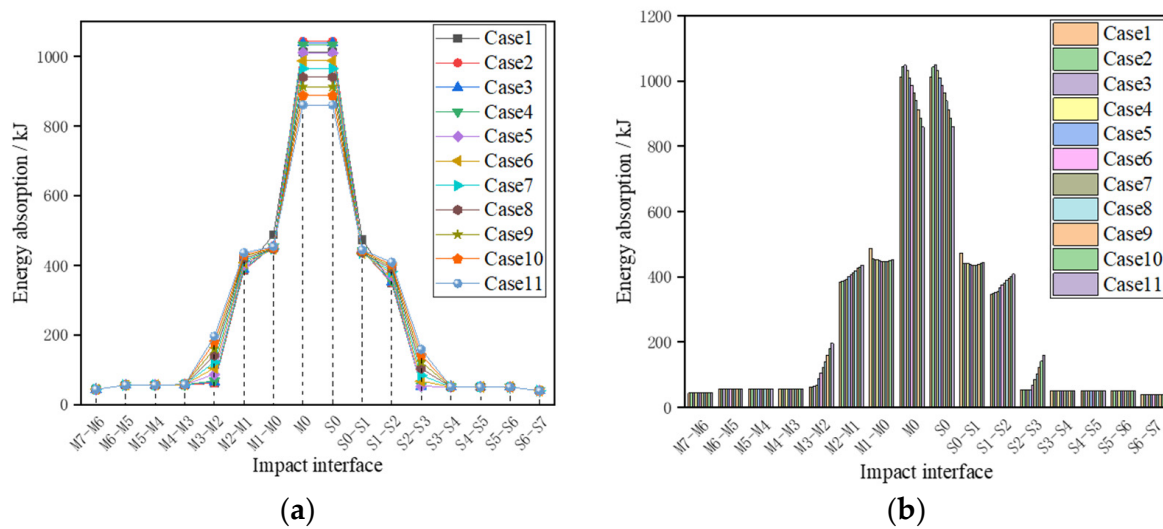


Figure 12. Influence of the platform force change on overall train collision energy: (a) broken line graph, (b) bar chart.

Figure 13a–d shows the change in the energy absorption of M0–S0, M1–M0, S0–S1, M2–M1, S1–S2, M3–M2 and S2–S3 with the variation in platform force F . From Figure 13a, it can be seen that, with the continuous increase in the platform force, the energy absorption of the head car increased first, and then decreased. This is because, in Case1–Case3, when the platform force of the energy-absorbing structure is low, the energy that can be absorbed by it is less, and part of the energy will be absorbed by the deformation of the vehicle body. Combined with Figure 14, when the platform force continues to vary, the energy-absorbing capacity of the structure become larger, and the car body is no longer compressed. Only the coupler buffer device and the anti-climbing device are used. The energy absorbed by the anti-climbing device gradually reduces, so the energy absorbed by the head car is reduced accordingly. Moreover, from Figure 14b, when the car body is deformed, the energy absorption of the first middle interfaces M1–M0 and S0–S1 will decrease rapidly with the increase in the platform force, and when the car body no longer has plastic deformation, its energy absorption will change slowly. It can also be seen from Figure 14c,d that the energy absorption of the second middle interfaces M1–M2 and S2–S1, and the third middle interfaces M2–M3 and S3–S2 will continue to increase significantly with the increase in the platform force.

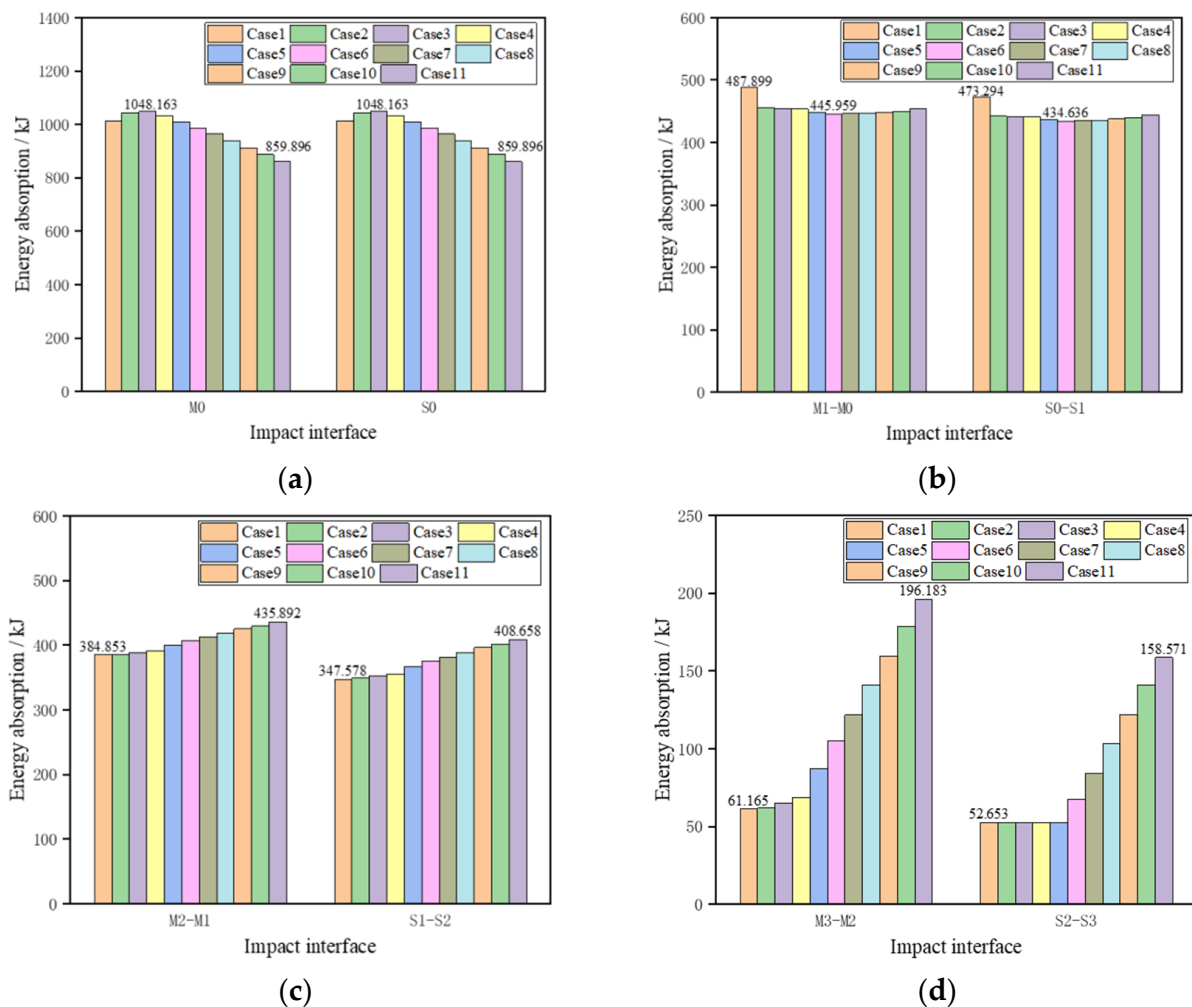


Figure 13. Influence of the platform force change on specific impact interfaces: (a) the head cars: M0 and S0; (b) the first middle car interfaces; (c) the second middle car interfaces; (d) the third middle car interfaces.

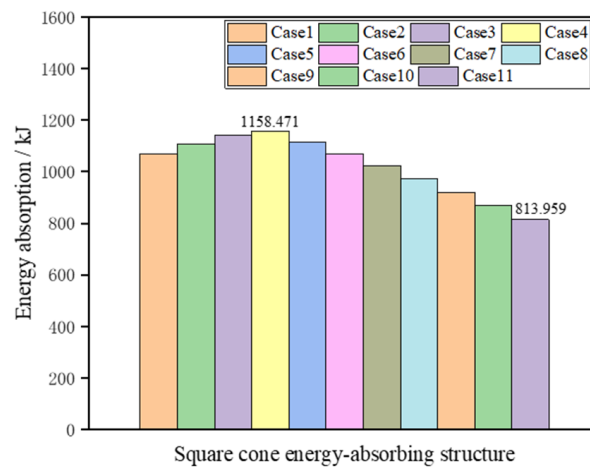


Figure 14. Influence of the platform force changes on square cone energy-absorbing structure.

In summary, and combined with Figure 15, when the platform force F of the energy-absorbing structure is low, the deformation of the car body will occur. The increase in F will reduce the energy absorbed by the first middle car interfaces $M1-M0$ and $S0-S1$ rapidly, and make the energy absorbed by the head cars and the second middle car interfaces $M2-M1$ and $S1-S2$ increase, while the interfaces of $M3-M2$ and $S2-S3$ will remain the same. With the further increase in the platform force, when the car body is no longer deformed, the energy absorption of $S0$ and $M0$ continues to reduce, and the energy absorption of $M1-M0$, $M2-M1$ and $M3-M2$, and $S0-S1$, $S1-S2$ and $S2-S3$ will all increase continuously.

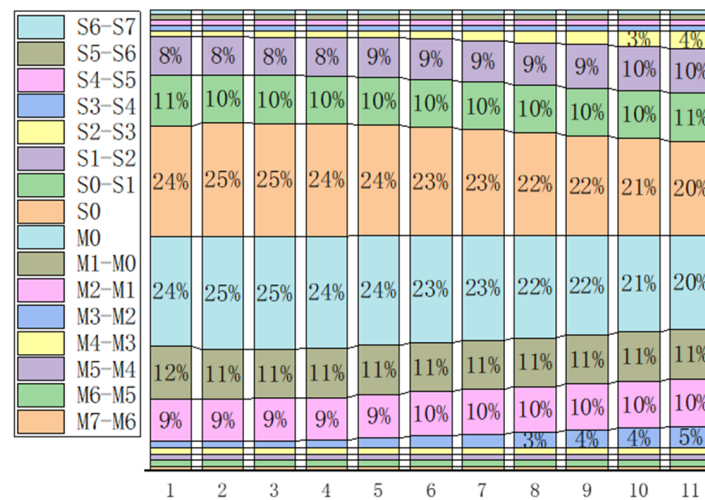


Figure 15. Energy distribution at each interface with the change in the platform force.

4.3. Influence of the Slope of Platform Force

Keeping the initial peak force $F_{max} = 2106$ kN and the platform force $F = 1650$ kN of the square cone anti-climbing energy-absorbing structure unchanged, and changing the slope of platform force K from 0.7 to 1.3 at intervals of 0.06 gives 11 sets of parameters Case1–Case11. The results of these calculations are shown in Figure 16. From Figure 16a, it is easy to identify, with the continuous increase in the platform force slope K , that the energy of seven impact interfaces that are closer to the collision center have obvious changes. Furthermore, from Figure 16b, we know that, with the increase in the slope of platform force, the energy absorption of the head cars continues to decrease, the energy of $M3-M2$, $M2-M1$, $M1-M0$, $S0-S1$, $S1-S2$ and $S2-S3$ interfaces all increase, and the energy absorption of the other interfaces remains basically invariable.

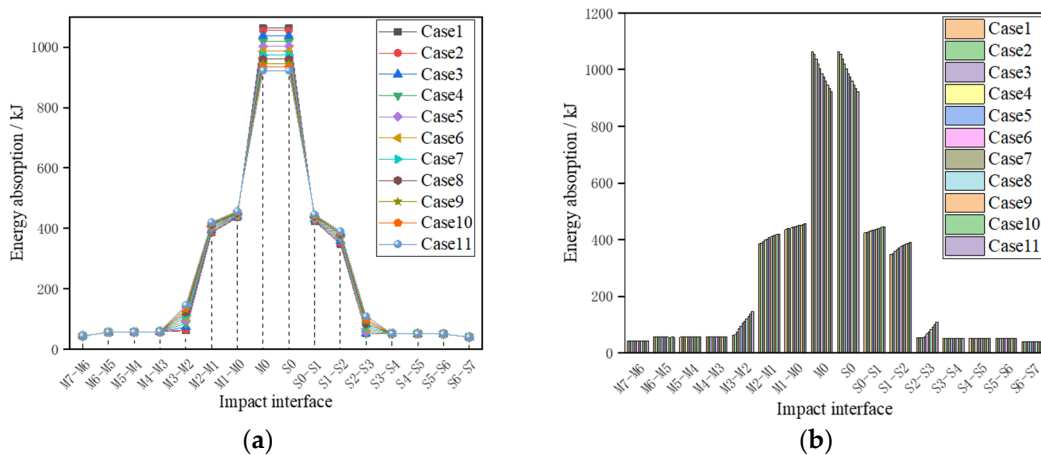


Figure 16. Influence of the slope of platform force change on overall train collision energy: (a) broken line graph, (b) bar chart.

The change in the energy absorption of impact interfaces that have obvious variation in the slope of the platform force is shown in Figure 17a–d. It can be seen from Figure 17a that the absorbed energy of the head cars decreases from 1040 kJ to 914 kJ continuously with the increase in the slope of platform force; combined with Figure 18, we know that there is no deformation of the head cars, and the energy absorption of the square cone energy-absorbing structure has the same trend as the head cars, which also decreases from 1184 kJ to 933 kJ with the variation in the slope. While, from Figure 18b–d, the trend of M1–M0, S0–S1, M2–M1, S1–S2, M3–M2 and S2–S3 is opposite; their energy absorption will become larger with the increase in the slope of platform force

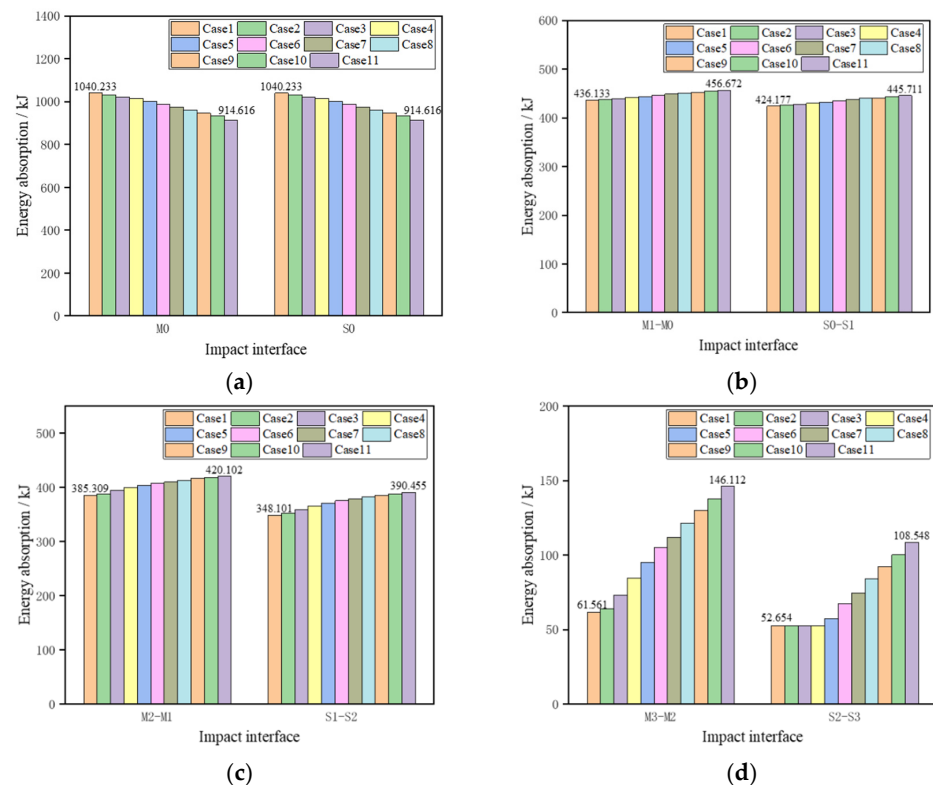


Figure 17. Influence of the slope of platform force change on specific impact interfaces: (a) the head cars: M0 and S0; (b) the first middle car interfaces; (c) the second middle car interfaces; (d) the third middle car interfaces.

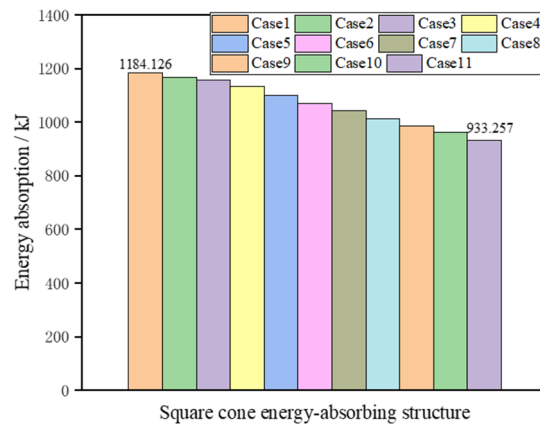


Figure 18. Influence of the slope of platform force changes on square cone energy-absorbing structure.

To sum up, according to Figure 19, it can be concluded that, under different collision conditions, with the increase in the force slope K , the energy absorption of the $S0$ and $M0$ vehicles decreases rapidly, and the energy absorption of the $M1-M0$, $M2-M1$, $M3-M2$, $S0-S1$, $S1-S2$ and $S2-S3$ impact interfaces increase, while the energy absorption of other interfaces remains basically invariable. This indicates that, with the increase in the slope K of the platform force, the energy absorption of the head car of the moving train and the stationary train will flow to the next three middle car impact interfaces, respectively.



Figure 19. Energy distribution at each interface with the change in the slope of platform force.

5. Multi-Objective Optimization Design

In a train collision, most of the energy will be absorbed by the energy-absorbing structure of vehicles that are closer to the collision interface. As the speed increases, the kinetic energy also increases rapidly. It often occurs that one interface absorbs too much energy, resulting in excessive deformation of the car body, and the energy absorbing structures of other interfaces are underutilized. From the above analysis, it can be seen that the energy-absorbing structure of six cars near the collision interface has basically been used up, and the absorbed energy of the subsequent interfaces are much lower. The multi-objective optimization problem in this paper can be expressed as: taking the energy absorption of the square cone anti-climbing energy-absorbing structure EA_{Anti} and the sum of the absorbed energy of the third middle car impact interfaces $EA_{M3} + EA_{S3}$ as optimization objectives, and the initial peak force F_{max} , platform force F , and platform force slope K are design variables. In order to generate a series of sample points, Hyperstudy and Motionview software were used for experimental design analysis and calculation separately, and then, taking the response surface method to build the surrogate model and fit the sample points, analyzing the influence of the design variables on the target. On this basis, the multi-objective genetic algorithm (MOGA) is used for the optimization

calculation to optimize the collision energy distribution. The constraints of this problem can be expressed as follows by mathematical methods:

$$\left\{ \begin{array}{l} \text{Max } EA_{\text{Anti}} \\ \text{Max } (EA_{S3} + EA_{M3}) \\ \text{s.t.} \\ 1906 \text{ kN} \leq F_{\text{max}} \leq 2306 \text{ kN} \\ 1450 \text{ kN} \leq F \leq 1850 \text{ kN} \\ 0.7 \leq K \leq 1.3 \end{array} \right. \quad (1)$$

5.1. Definition of Optimization Problems

Design of experiment (DOE) refers to a research method based on theories such as probability theory and mathematical statistics, taking economical and scientific arrangement of the experimental plan to obtain the relationship between the target response and the experimental factors. The D-optimal method, partial factor method, full factor method, central composite method, Box-Behnken method [30], Latin hypercube method, optimized Latin hypercube [31], Hammersley method et al. are commonly used experimental design methods in the process of experimental design. Considering that the response surface model involved in this paper may have a high degree of nonlinearity, and the Hammersley method can obtain a better uniform distribution on the multi-dimensional hypercube and it has been proven to have good application effect for nonlinear problems, the Hammersley method was applied in this paper. According to the three design variables and two objective responses, the experimental design produced a total of 150 sample points, some of which are shown in Table 3.

Table 3. Simulation results.

NO.	Design Variables			Objective Responses	
	Fmax (kN)	F (kN)	K	EA _{Anti} (kJ)	EA _{M3} + EA _{S3} (kJ)
1	1907.333	1650.000	1.095	1168.056	140.724
2	1910.000	1550.000	0.762	1090.335	165.814
3	1912.667	1750.000	1.266	1197.483	136.907
4	1915.333	1600.000	0.817	1164.991	128.919
5	1918.000	1700.000	0.913	1016.583	241.729
6	1920.667	1675.000	1.087	1222.256	118.361
7	1923.333	1800.000	1.183	1009.102	258.380
8	1926.000	1475.000	0.728	1076.205	168.505
9	1928.667	1675.000	1.299	1223.757	116.445
10	1931.333	1625.000	0.967	1177.866	129.140
...
150	2304.667	1614.625	1.070	1200.716	128.544

5.2. Building a Surrogate Model

The commonly used methods for constructing surrogate models include the radial basis function (RBF), polynomial response surface method (PRSM) [32], moving least squares method (MLSM), artificial neural network [33] and Kriging model [34], etc. Due to the nonlinearity of the problem addressed in this paper, it is difficult to derive the objective function analytically. The radial basis function (RBF) method has been identified to have good application prospects for highly nonlinear problems, so RBF was used to construct surrogate models. In addition, 30 sets of sample points were generated by using the Latin hypercube method to verify the accuracy of the surrogate model.

Figures 20 and 21 show the response surface diagram of the surrogate model constructed by radial basis functions and its interaction coupling relationship. As can be seen from Figure 20, for the platform force F and initial peak force F_{max}, the former has an obviously greater impact on EA_{Anti} than the latter. EA_{Anti} will decrease with the increase

in platform force F , while the initial peak force has little influence on it. For the slope of platform force K and the initial peak force F_{max} , the effects of these two variables on EA_{Anti} are about the same as the former. The influence of the slope is larger than the initial peak force, its increase will lead to the decrease in EA_{Anti} , and with the variation in F_{max} , EA_{Anti} will decrease a little first and then increase, but the change is marginal. From Figure 20c, it can be seen that both the platform force F and the slope K have obvious effects on EA_{Anti} , and EA_{Anti} will increase first and then decrease with the change in these variables. The influence of three variables on the response of $EA_{M3} + EA_{S3}$ are shown in Figure 21. It is easy to see that the platform force and the slope have a great effect on the response, while the initial peak force has little impact on it, and $EA_{M3} + EA_{S3}$ becomes obviously larger with the increase in the platform force and the slope.

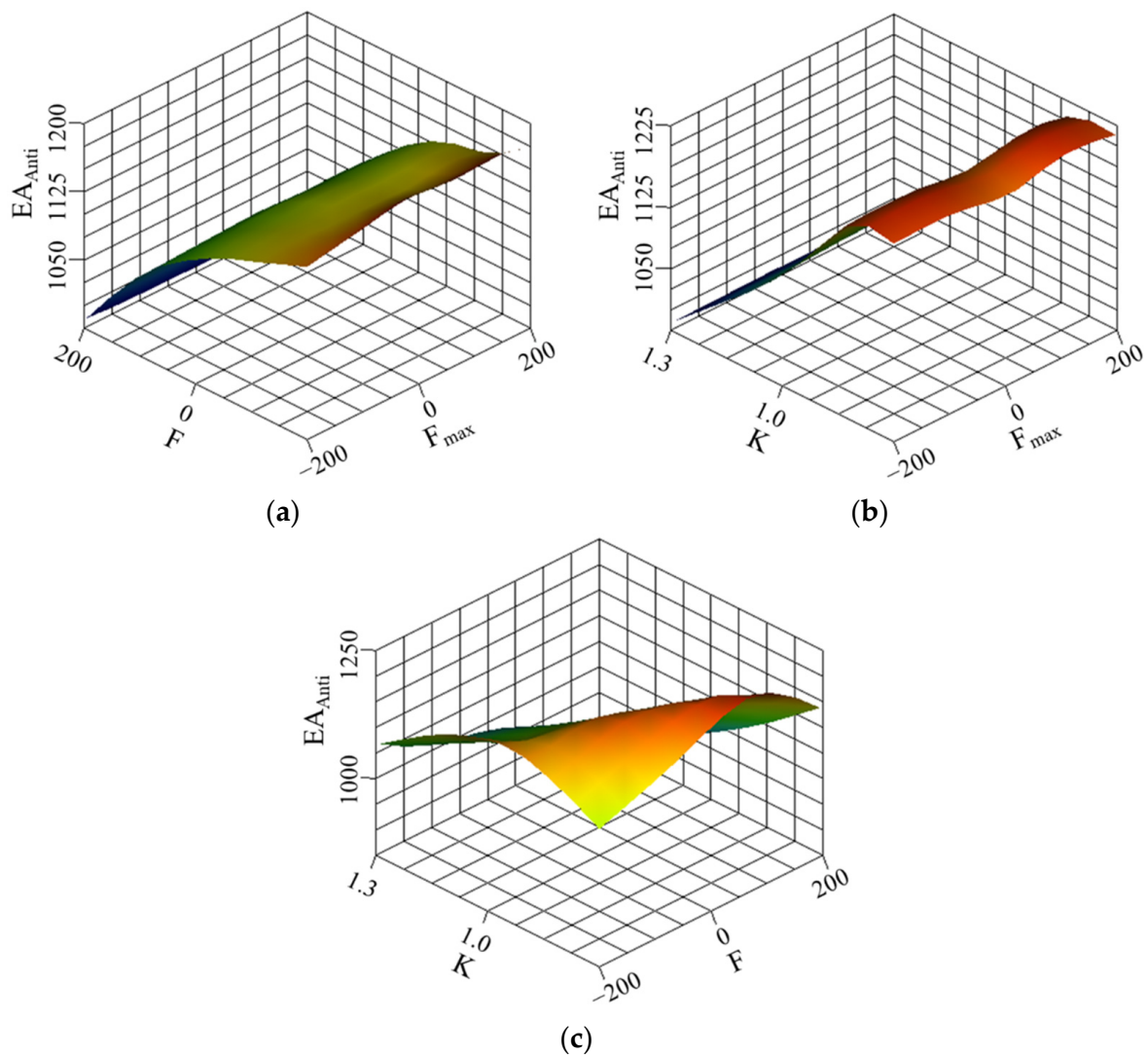


Figure 20. Influence of three variables on EA_{Anti} : (a) F and F_{max} ; (b) K and F_{max} ; (c) K and F .

Figure 22 depicts a regression plot of 30 sets of test data to represent the correlation between the surrogate model constructed by radial basis functions and dynamic simulation. It can be seen from the figure that the points of the predicted value of the surrogate model and the calculated value of the dynamic simulation are distributed near the 45-degree line, indicating that the accuracy of the surrogate model is great and the results are reliable, which can be used for further research.

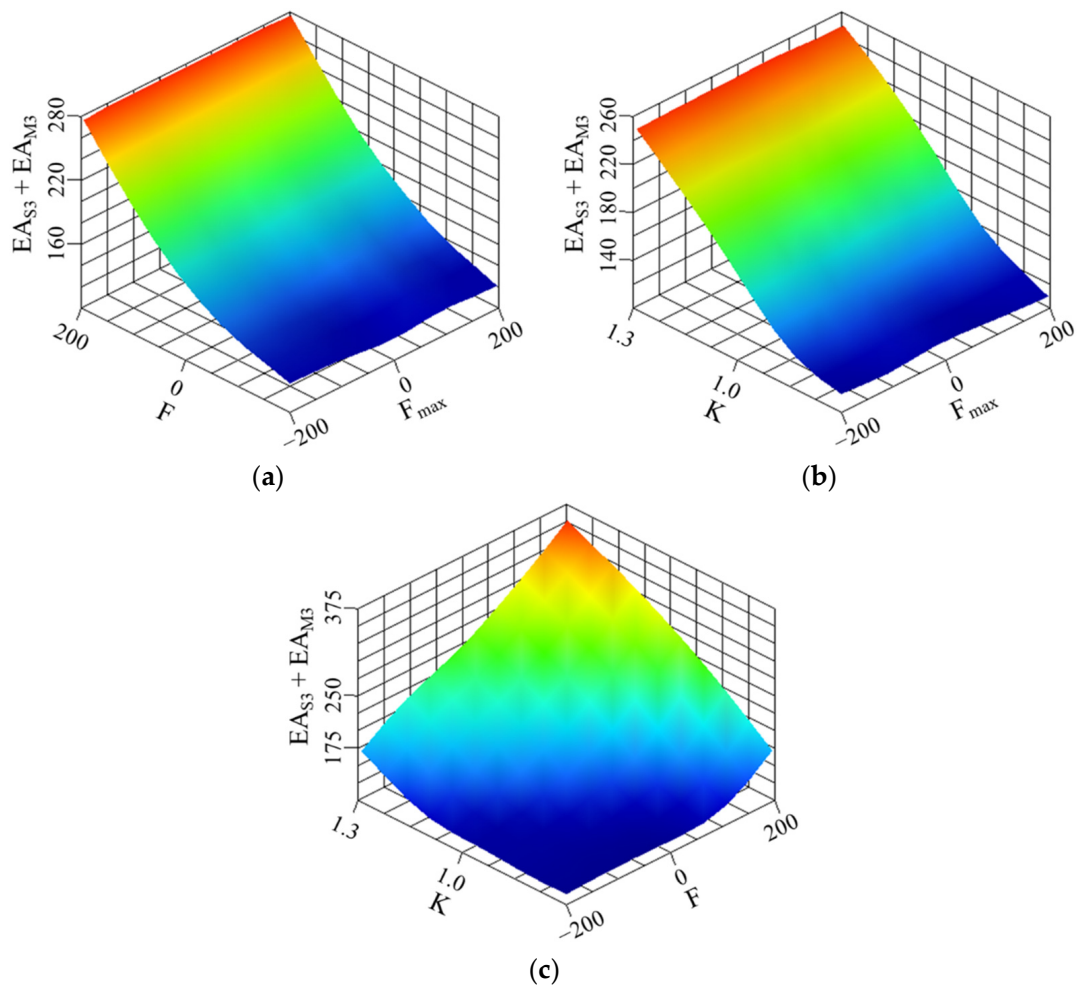


Figure 21. Influence of three variables on $EA_{M3} + EA_{S3}$: (a) F and F_{max} ; (b) K and F_{max} ; (c) K and F .

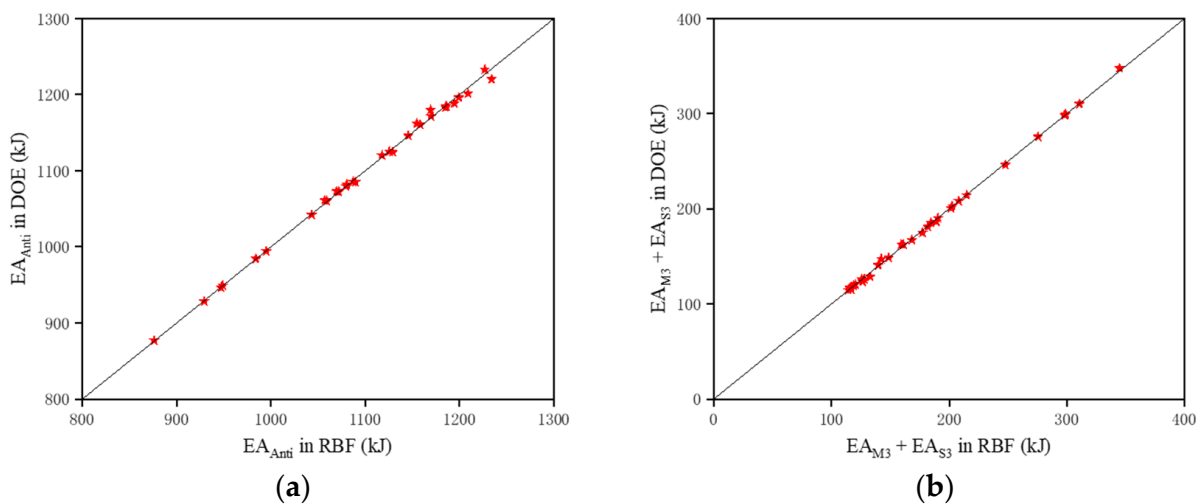


Figure 22. Regression plot for responses: (a) EA_{Anti} ; (b) $EA_{M3} + EA_{S3}$.

In addition, we also used three common evaluation parameters, average relative error (ARE), coefficient of determination (R^2), and relative average absolute error (RAAE) to

verify the accuracy of the surrogate model, respectively. The specific expressions of these evaluation parameters are as follows:

$$ARE = \frac{\sum \frac{|\hat{y}_i - y_i|}{y_i}}{n} \times 100\% \quad (2)$$

$$R^2 = 1 - \frac{\sum (\hat{y}_i - y_i)^2}{\sum (\hat{y}_i - \bar{y}_i)^2} \quad (3)$$

$$RAAE = \frac{\frac{1}{n} \sum_{i=1}^n |y_i - \hat{y}_i|}{\sqrt{\frac{1}{n} \sum_{i=1}^n |y_i - \bar{y}_i|^2}} \quad (4)$$

In these formulae, n is the number of sample points and y_i and \hat{y}_i are the simulation calculation value and the predicted value by the surrogate model, respectively. In addition, \bar{y}_i is the average of simulation response values for all sample points. The closer the value of the coefficient of determination R^2 is to 1 indicates that the constructed surrogate model has a higher prediction accuracy, which is the same for ARE and $RAAE$, if these two parameters are closer to 0. The values of these three evaluation parameters for surrogate models are shown in Table 4; it can be seen that both the coefficient of determination for EA_{Anti} and $EA_{M3} + EA_{S3}$ are larger than 0.99, and the other two parameters are all closer to 0, indicating that the surrogate model constructed by radial basis function is accurate, which can guarantee the reliability of the results based on the model.

Table 4. Surrogate model accuracy evaluation parameters.

Evaluation Parameters	EA_{Anti}	$EA_{M3} + EA_{S3}$
ARE (%)	0.015	0.161
R^2	0.997	0.995
RAAE (%)	0.033	0.020

5.3. Optimization Algorithm

In optimization problems, we often choose the genetic algorithm (GA) to solve, and for multi-objective optimization problems, Fonseca and Fleming first proposed a multi-objective genetic algorithm for non-inferior classification of genetic algorithm populations in 1993, the multiple objective genetic algorithm (MOGA), which uses a general genetic algorithm framework to efficiently solve multi-objective problems [35]. In the multi-objective optimization problem in this paper, there is more than one objective function to be minimized or maximized. The goal is not to find the optimal value, but to get the pareto-optimal set for EA_{Anti} and $EA_{M3} + EA_{S3}$. The flow chart of the MOGA algorithm used in this paper is shown in Figure 23, and the relevant parameter design is shown in Table 5.

Table 5. Relative parameters of MOGA.

Parameters	Value
Maximum Iterations	50
Minimum Iterations	25
Population Size	70
Mutation Rate	0.01
Elite Population (%)	10
Random Seed	1
Distribution Index	5

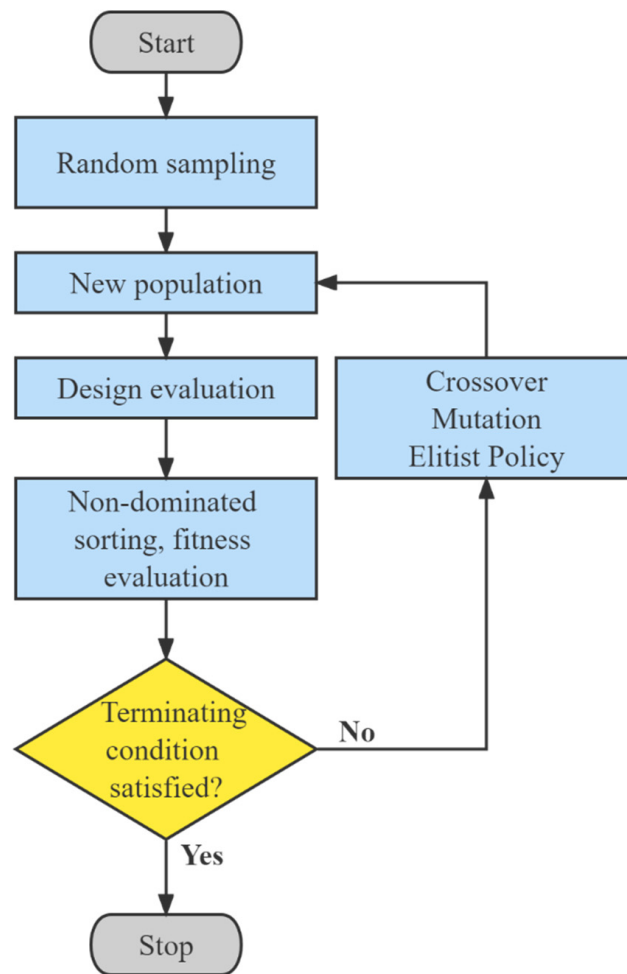


Figure 23. The flow of the MOGA algorithm.

5.4. Optimization Result

The Pareto set obtained according to the MOGA algorithm is shown in Figure 24. It can be seen from the figure that the increase in energy absorption of the square cone anti-climbing structure EA_{Anti} and the increase in the sum of energy absorption of the third middle car interfaces $EA_{M3} + EA_{S3}$ are conflicting with each other. When EA_{Anti} increases, $EA_{M3} + EA_{S3}$ will decrease. The variation in $EA_{M3} + EA_{S3}$ will also lead to the opposite change in EA_{Anti} . In order to select the most satisfactory scheme from Pareto solution set, a multi-criteria decision-making method is usually used to allocate the weights of multiple objectives to emphasize their importance and then build a comprehensive evaluation model, such as the order relation method, grey-related method [36], etc. However, in this paper, it is difficult to assign appropriate weights to the two targets. This paper uses the minimum distance selection method (TMDSM) [37], which does not need to assign weights to the targets, but evaluates the scheme through the distance from the ideal point. It can be expressed by mathematical formula as the following:

$$\min D = \sqrt{\sum_{n=1}^M (f_{in} - \min(f_n(x)))^2} \quad (5)$$

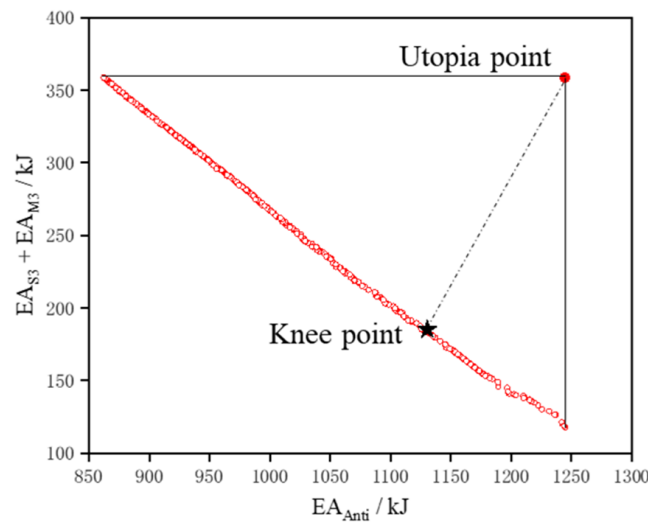


Figure 24. Pareto frontier and optimal scheme of multi-objective optimization.

In this formula, D is the distance from the optimal solution (knee point) to the ideal point (utopia point), f_{in} is the value of the objective function n corresponding to the i th solution in the Pareto solution set and M is the number of objective functions.

The best optimal scheme in the Pareto solution set obtained by the minimum distance selection method through MOGA is also shown in Figure 24, in which the scheme corresponding to the optimal solution is $F_{max} = 1910.739$ kN, $F = 1849.373$ kN and $K = 0.751$, and the corresponding is $EA_{Anti} = 1131.937$ kJ and $EA_{M3} + EA_{S3} = 188.106$ kJ.

Putting the set of parameters obtained by the optimization algorithm into the dynamic model for calculation, the optimization calculation result is obtained, which is shown in Table 6. Comparing the optimization scheme and the optimization calculation result, it can be found that the error is very small, which shows that the optimization method is reliable. Comparing the optimization calculation result based on the optimization scheme with the initial calculation, we know that EA_{Anti} increased by 1.31% and $EA_{M3} + EA_{S3}$ increased by 9.17%, and it can be further found from Figure 25 that the energy absorption of the head car collision interface in the optimization scheme increased slightly by 0.74%, the energy absorption of the first middle car collision interfaces (M1–M0 and S0–S1) decreased significantly by 3.36%, the energy absorption of the second middle car collision interfaces (M2–M1 and S1–S2) remained basically unchanged and the energy absorption of the third middle car collision interfaces (M3–M2 and S2–S3) increased significantly by 9.17%. The train collision energy distribution should be more reasonable. Because the energy absorption of the first middle car collision interfaces was reduced, the compression deformation of their car body was reduced, which can better protect the safety of passengers and the structural integrity of the vehicle; at the same time, the energy absorption of the third collision interfaces was improved, so the utilization efficiency of the subsequent energy absorption structure was improved.

Table 6. Comparison of results before and after optimization.

	Fmax/kN	F/kN	K	EA _{Anti} /kJ	EA _{M3} + EA _{S3} /kJ
Optimization scheme	1910.739	1849.373	0.715	1131.937	187.106
Optimization calculation	The same	The same	The same	1130.530	188.133
Initial calculation	2106.000	1650.000	1.000	1115.985	172.326
Variation	/	/	/	1.31%	9.17%

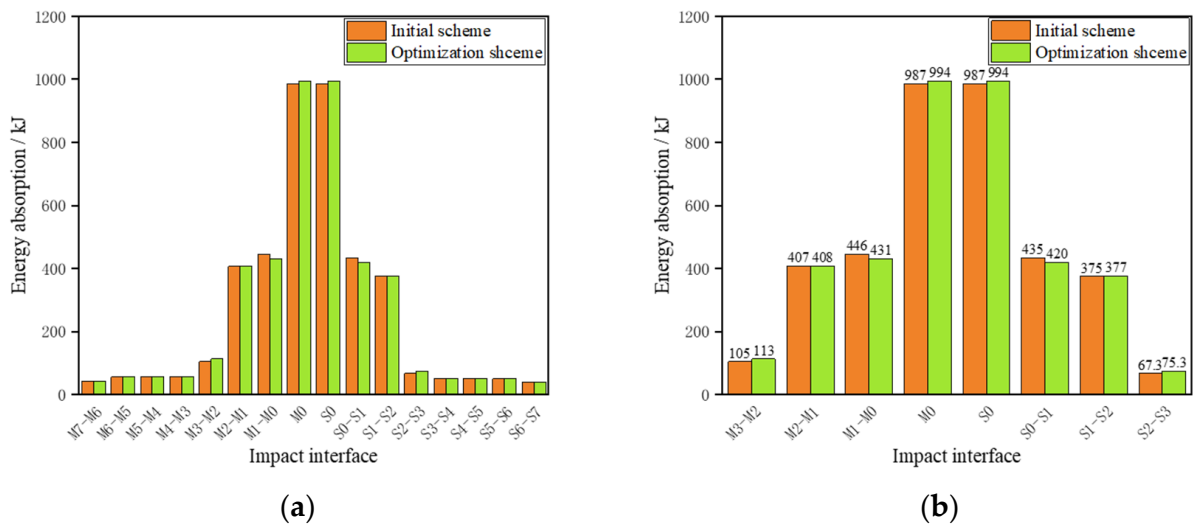


Figure 25. Comparison of energy distribution results before and after optimization: (a) all impact interfaces; (b) specific impact interfaces.

6. Conclusions

In this paper, we established the train collision dynamic model, and then obtained the force displacement characteristic curve of the square cone energy-absorbing structure through the impact experiment. Based on this curve, three mechanical characteristic parameters: the initial peak force, platform force and slope of the curve, were extracted from it, and the effects of the changes of three parameters on the train collision energy distribution under the collision scenario of 25 km/h were studied. To find the optimal design of these parameters, the response surrogate model was constructed, and the MOGA algorithm was used in optimization calculations. The main conclusions are as follows:

- The changes in the initial peak force F_{max} , platform force F and platform force slope K of the square cone energy-absorbing structure have an influence on the distribution of train collision energy, which is mainly concentrated in M3–M2, M2–M1, M1–M0, M0–S0, S0–S1, S1–S2 and S2–S3 interfaces, but the degree was different. The changes in the platform force and platform force slope have a greater influence, while the initial peak force has a smaller impact.
- The increase in the initial peak force F_{max} will reduce the energy absorption of the middle car impact interfaces M1–M0 and S0–S1, and increase the energy absorption of M0–S0. However, it has no influence on the energy absorption of other impact interfaces.
- When the platform force F is small, the head car body participates in energy absorption; its increase will lead to a rapid decrease in the energy absorption of M1–M0 and S0–S1, and an increase in M0–S0, M2–M1 and S1–S2 impact interfaces. When F is large, the deformation of the head car body will no longer occur, and the energy absorption of M0–S0 will reduce, and the other six impact interfaces will increase with its increase.
- For the platform force slope K , an increase will reduce the energy absorption of the head car collision interface M0–S0, and the subsequent energy absorption of M3–M2, M2–M1, M1–M0, S0–S1, S1–S2 and S2–S3 will increase continuously, which means that the collision energy will be dispersed from two head cars to the following six middle car collision interfaces.
- Compared with the initial calculation, the optimization scheme has the more reasonable energy distribution. The energy absorption of the head car collision interface increases, the energy absorption of the first middle car impact interfaces decreases, and the third middle car impact interfaces obviously increase. The utilization efficiency of the energy-absorbing structure is improved.

Author Contributions: Conceptualization, P.X. and A.W.; methodology, A.W., P.X. and C.Y.; software, A.W.; investigation, A.W. and Q.C.; resources, A.W., Q.C. and L.Y.; experiment, Q.C.; data curation, P.X., L.Y. and A.W.; writing, A.W. and C.Y.; funding acquisition, P.X. and C.Y. All authors have read and agreed to the published version of the manuscript.

Funding: The authors would like to acknowledge the financial support from the Changsha Municipal Natural Science Foundation [No. kq2202102], the Hunan Provincial Natural Science Foundation of China (No. 2022JJ40619), the National Key Research and Development Program of China [No. 2021YFB3703801, 2021YFB3703801-02, 2021YFB3703801-04], the Scientific Research Foundation for Young Scholars of Central South University [No. 202044019], and the Leading Talents of Science and Technology of Hunan Province [No. 2019RS3018].

Institutional Review Board Statement: Not applicable.

Informed Consent Statement: Not applicable.

Data Availability Statement: Not applicable.

Conflicts of Interest: The authors declare no conflict of interest.

Abbreviations

F_{\max}	Initial peak force
F	Platform force
K	Slope of platform force
EA	Energy absorption
EA_{Anti}	Energy absorption of the square cone anti-climbing structure
$EA_{M3} + EA_{S3}$	Energy absorption of the third middle car impact interfaces (i.e., M3–M2 and S2–S3)
DOE	Design of experiment
RS	Response surface
RBF	Radial basis function
MOGA	Multiple objective genetic algorithm
TMDSM	The minimum distance selection method

References

- Gao, G.; Zhuo, T.; Guan, W. Recent research development of energy-absorption structure and application for railway vehicles. *J. Cent. South Univ.* **2020**, *27*, 1012–1038. [\[CrossRef\]](#)
- Marzbanrad, J.; Mehdikhanlo, M.; Saeedi Pour, A. An energy absorption comparison of square, circular and elliptic steel and aluminum tubes under impact loading. *Turk. J. Eng. Environ. Sci.* **2010**, *33*, 159–166. [\[CrossRef\]](#)
- Alavi Nia, N.; Parsapour, M. An investigation on the energy absorption characteristics of multi-cell square tubes. *Thin-Walled Struct.* **2013**, *68*, 26–34. [\[CrossRef\]](#)
- Song, J.; Chen, Y.; Lu, G. Axial crushing of thin-walled structures with origami patterns. *Thin-Walled Struct.* **2012**, *54*, 65–71. [\[CrossRef\]](#)
- Goyal, S.; Anand, C.S.; Sharma, S.K.; Sharma, R.C. Crashworthiness analysis of foam filled star shape polygon of thin-walled structure. *Thin-Walled Struct.* **2019**, *144*, 6312. [\[CrossRef\]](#)
- Yao, S.; Zhou, Y.; Li, Z.; Zhang, P.; Cao, Y.; Xu, P. Energy absorption characteristics of square frustum lattice structure. *Compos. Struct.* **2021**, *275*, 4492. [\[CrossRef\]](#)
- Zhang, X.; Zhang, H. Energy absorption of multi-cell stub columns under axial compression. *Thin-Walled Struct.* **2013**, *68*, 156–163. [\[CrossRef\]](#)
- Kannan, I.V.; Rajkumar, R. Deformation and energy absorption analysis of simple and multi-cell thin-walled tubes under quasi-static axial crushing. *Int. J. Crashworthiness* **2020**, *25*, 121–130. [\[CrossRef\]](#)
- Gao, G.; Dong, H.; Tian, H. Collision performance of square tubes with diaphragms. *Thin-Walled Struct.* **2014**, *80*, 167–177. [\[CrossRef\]](#)
- Yao, S.; Xiao, X.; Xu, P.; Qu, Q.; Che, Q. The impact performance of honeycomb-filled structures under eccentric loading for subway vehicles. *Thin-Walled Struct.* **2018**, *123*, 360–370. [\[CrossRef\]](#)
- Xie, S.; Du, X.; Zhou, H.; Wang, J.; Chen, P. Crashworthiness of Nomex honeycomb-filled anti-climbing energy absorbing devices. *Int. J. Crashworthiness* **2021**, *26*, 121–132. [\[CrossRef\]](#)
- Xu, P.; Yang, C.; Peng, Y.; Yao, S.; Xing, J.; Li, B. Cut-out grooves optimization to improve crashworthiness of a gradual energy-absorbing structure for subway vehicles. *Mater. Des.* **2016**, *103*, 132–143. [\[CrossRef\]](#)
- Wang, J.; Lu, Z.; Zhong, M.; Wang, T.; Sun, C.; Li, H. Coupled thermal–structural analysis and multi-objective optimization of a cutting-type energy-absorbing structure for subway vehicles. *Thin-Walled Struct.* **2019**, *141*, 360–373. [\[CrossRef\]](#)

14. Chen, J.; Liang, X.; Xu, P.; Che, Q. Windowed design and structure optimization of energy absorbing structure of high-speed train. *J. Railw. Sci. Eng.* **2022**, *19*, 1502–1510. [[CrossRef](#)]
15. Guo, W.; Xu, P.; Yi, Z.; Xing, J.; Zhao, H.; Yang, C. Variable Stiffness Design and Multiobjective Crashworthiness Optimization for Collision Post of Subway Cab Cars. *Machines* **2021**, *9*, 246. [[CrossRef](#)]
16. Lu, G. Energy absorption requirement for crashworthy vehicles. *Proc. Inst. Mech. Eng. Part F J. Rail Rapid Transit* **2002**, *216*, 31–39. [[CrossRef](#)]
17. Sun, Y.Q.; Cole, C.; Thambiratnam, D.P. Modeling and Analysis of the Crush Zone of a Typical Australian Passenger Train. *Veh. Syst. Dyn.* **2012**, *50*, 1137–1155. [[CrossRef](#)]
18. Gao, G. The energy distribution of a train impact process based on the active–passive energy-absorption method. *Transp. Saf. Environ.* **2019**, *1*, 54–67. [[CrossRef](#)]
19. Yao, S.; Yan, K.; Lu, S.; Xu, P. Energy-absorption optimisation of locomotives and scaled equivalent model validation. *Int. J. Crashworthiness* **2022**, *4*, 441–452. [[CrossRef](#)]
20. Zhao, H.; Xu, P.; Jiang, S.; Li, B.; Yao, S.; Xing, J.; Huang, Q.; Xu, K. A novel design method of the impact zone of a high-speed train. *Int. J. Crashworthiness* **2020**, *27*, 476–485. [[CrossRef](#)]
21. Ambrósio, J. Crash Analysis and Dynamical Behaviour of Light Road and Rail Vehicles. *Veh. Syst. Dyn.* **2005**, *43*, 385–411. [[CrossRef](#)]
22. Xu, P.; Lu, S.; Yan, K.; Yao, S. Energy absorption design study of subway vehicles based on a scaled equivalent model test. *Proc. IMechE Part F J. Rail Rapid Transit* **2019**, *23*, 3–15. [[CrossRef](#)]
23. European Committee for Standardization. *EN 15227: 2020, Railway Applications Crashworthiness Requirements for Railway Vehicle Bodies*; British Standard Published: London, UK, 2020.
24. Federal Railroad Administration. *Improving Railroad Safety and Rail Passenger Technology Through Targeted Research and Demonstrations, 1992–1997*; US Department of Transportation: Washington, DC, USA, 1999.
25. Carolinev, D. *Passenger Rail Train-to-Train Impact Test Volume II: Summary of Occupant Protection Program*; US Department of Transportation: Washington, DC, USA, 2003.
26. Lyu, T.; Xiao, S.; Zhu, T.; Zhang, J.; Wang, X.; Li, Y.; Yang, G.; Yang, B. Optimization of Train Crash Energy Allocation Scheme with Multi-objective Evolutionary Algorithm. *China Mech. Eng.* **2021**, *32*, 2262–2267. [[CrossRef](#)]
27. Zhang, J.; Zhu, T.; Wang, X.; Xiao, S.; Yang, G.; Yang, B. Comprehensive Evaluation Model for One-Dimensional Crash Energy Management of Trains. *J. Southwest Jiaotong Univ.* **2021**, *56*, 1329–1336. [[CrossRef](#)]
28. Wang, D.; Xu, P.; Yang, C.; Xiao, X.; Che, Q. Crashing performance and multi-objective optimization of honeycomb-filled thin-walled energy absorber with axisymmetric thickness. *Mech. Adv. Mater. Struct.* **2022**. [[CrossRef](#)]
29. Xu, P.; Yang, L.; Yao, S.; Guo, W.; Che, Q.; Wang, A. Collision mechanics parameter design and multi-objective optimization of square cone anti-climbing energy-absorbing structure for urban rail trains. *J. Cent. South Univ. (Sci. Technol.)* **2022**, *53*, 1689–1699. [[CrossRef](#)]
30. Ferreira, S.L.C.; Bruns, R.E.; Ferreira, H.S.; Matos, G.D.; David, J.M.; Brandão, G.C.; da Silva, E.G.P.; Portugal, L.A.; dos Reis, P.S.; Souza, A.S.; et al. Box-Behnken Design: An Alternative for the Optimization of Analytical Methods. *Anal. Chim. Acta* **2007**, *597*, 179–186. [[CrossRef](#)]
31. Xu, P.; Qu, C.; Yao, S.; Yang, C.; Wang, A. Numerical Optimization for the Impact Performance of a Rubber Ring Buffer of a Train Coupler. *Machines* **2021**, *9*, 225. [[CrossRef](#)]
32. Zhao, H.; Xu, P.; Li, B.; Yao, S.; Yang, C.; Guo, W.; Xiao, X. Full-Scale Train-to-Train Impact Test and Multi-Body Dynamic Simulation Analysis. *Machines* **2021**, *9*, 297. [[CrossRef](#)]
33. Prasanna, J.; Karunamoorthy, L.; Venkat Raman, M.; Prashanth, S.; Raj Chordia, D. Optimization of process parameters of small hole dry drilling in Ti-6Al-4V using Taguchi and grey relational analysis. *Measurement* **2014**, *48*, 346–354. [[CrossRef](#)]
34. Zhang, Y.; Xu, X.; Sun, G.; Lai, X.; Li, Q. Nondeterministic optimization of tapered sandwich column for crashworthiness. *Thin-Walled Struct.* **2018**, *122*, 193–207. [[CrossRef](#)]
35. Xu, P.; Xing, J.; Yao, S.; Yang, C.; Chen, K.; Li, B. Energy distribution analysis and multi-objective optimization of a gradual energy-absorbing structure for subway vehicles. *Thin-Walled Struct.* **2017**, *115*, 255–263. [[CrossRef](#)]
36. Tosun, N. Determination of Optimum Parameters for Multi-Performance Characteristics in Drilling by Using Grey Relational Analysis. *Int. J. Adv. Manuf. Technol.* **2006**, *28*, 450–455. [[CrossRef](#)]
37. Xu, P.; Zhao, H.; Yao, S.; Che, Q.; Xing, J.; Huang, Q.; Xu, K. Multi-objective optimisation of a honeycomb-filled composite energy absorber for subway vehicles. *Int. J. Crashworthiness* **2019**, *25*, 603–611. [[CrossRef](#)]